

A quantized anomalous Hall effect above 4.2 K in stacked topological insulator/magnet bilayers

Authors: Rakshit Jain^{1,2,3*}, Matthew Roddy¹, Vishakha Gupta¹, Benjamin Huang¹, Hasan M. Sayeed⁴, Husain F. Alnaser⁴, Amit Vashist⁴, Kenji Watanabe⁵, Takashi Taniguchi⁶, Vikram V. Deshpande⁴, Taylor D. Sparks⁴, Daniel C. Ralph^{1,3*}

Affiliations:

¹Department of Physics, Cornell University, Ithaca, NY 14853, USA.

²School of Engineering and Applied Physics, Cornell University, Ithaca, NY 14853, USA.

³Kavli Institute for Nanoscale Science, Cornell University, Ithaca, NY 14853, USA.

⁴University of Utah, Salt Lake City, UT 84112, USA.

⁵Research Center for Electronic and Optical Materials, National Institute for Materials Science Tsukuba, Ibaraki 305-0044, Japan.

⁶Research Center for Materials Nanoarchitectonics, National Institute for Materials Science Tsukuba, Ibaraki 305-0044, Japan.

*Corresponding authors. Emails: rj372@cornell.edu; dcr14@cornell.edu

Abstract: Quantized anomalous Hall effects (QAHEs) occur in remarkable electronic states which possess not only quantized Hall signals but in some cases regions of dissipationless electron transport. The initial demonstrations of a QAHE in a magnetically-doped topological insulator (TI) required temperatures below 100 mK, and since then a major focus of the field has been to increase the temperature scale. Here, we report quantized Hall signals up to 10 K (in what is known as the parity anomaly state) in TI/magnet bilayers made by mechanical assembly, rather than by conventional deposition techniques. This is a factor of 100 higher temperature than any previous realization of a QAHE in a proximity-coupled TI/magnet heterostructure made by deposition, and approximately twice the previous record for any QAHE system.

Main Text:

To create a quantized anomalous Hall effect (QAHE), one must combine a materials system containing topological electron bands with magnetic interactions that induce an exchange gap in the topological surface state; a quantized Hall signal can be achieved (even with zero applied magnetic field) when the Fermi level is tuned to lie within the exchange gap (1–5). A QAHE was first observed in topological insulators in which magnetic dopant atoms provide the necessary magnetic interactions (6, 7), but originally only at temperatures below 100 mK. Increasing the temperature at which QAHEs can be realized is necessary before this fascinating effect can be utilized for technologies such as resistance standards, dissipation-free channels, and non-reciprocal circuit components, as well as for more detailed fundamental studies (3–5, 8).

Three flavors of the QAHE have been realized in magnetically-doped topological insulators (Fig. 1(a)) (2–5), all with similar temperature scales: (i) when only one surface of a topological-insulator thin film is gapped by magnetic interactions, the Hall conductivity can achieve the value $\sigma_{xy} = e^2/2h$ (where e is the electric charge and h is Planck’s constant), known as the parity anomaly state (9, 10); (ii) when both surfaces of a topological insulator film are gapped by magnets with aligned magnetizations, the Hall conductivities of the two interfaces add to give $\sigma_{xy} = e^2/h$, known as the Chern insulator state or the integer quantum anomalous Hall effect; and (iii) when both surfaces of a topological insulator are gapped by magnets with anti-aligned magnetizations, the Hall conductivities of the two interfaces subtract to give $\sigma_{xy} = 0$, known as the axion insulator state.

Extensive efforts at improving sample quality in magnetically-doped topological insulators have increased the temperature scale of their QAHEs to 2 K using modulation doping (11) or magnetic co-doping (12), and more recently to approximately 4-5 K when Mn impurities self-organize into a superlattice (13) or with a CrO_x capping layer (14). QAHEs have also now been observed in $\text{Zn}_{1-x}\text{Cr}_x\text{Te}/(\text{Bi}_{1-y}\text{Sb}_y)_2\text{Te}_3/\text{Zn}_{1-x}\text{Cr}_x\text{Te}$ samples (15), exfoliated flakes of the intrinsic topological antiferromagnet MnBi_2Te_4 (16, 17), twisted bilayer graphene (18, 19), ABC trilayer graphene (20), and $\text{MoTe}_2/\text{WSe}_2$ bilayers (21), and very recently fractional QAHEs have been detected in moiré systems (22–24), but the upper temperature limit for these QAHEs has remained stubbornly low, less than or equal to about 2 K in all of these other systems.

A frequently-attempted strategy for enhancing the temperature scale of QAHEs has been to try to create a large exchange gap using the magnetic proximity effect in topological insulator/magnet heterostructures, instead of using disordered magnetic dopants (references (25) and (26) provide excellent reviews). Density functional calculations for van der Waals topological insulator/ magnet structures predict exchange gaps as large as several tens of meV, suggesting the possibility that QAHEs should be observable in proximity-coupled heterostructures at least up to several 10’s of Kelvin (27–29). However, previous experiments which grew proximity-coupled samples by molecular beam epitaxy or other top-down deposition techniques have generally not been able to achieve a QAHE (25, 26, 30–36). We are aware of only one demonstration of a QAHE using proximity coupling in deposited structures, in $\text{Zn}_{1-x}\text{Cr}_x\text{Te}/(\text{Bi}_{1-y}\text{Sb}_y)_2\text{Te}_3/\text{Zn}_{1-x}\text{Cr}_x\text{Te}$ samples (15) at temperatures below 100 mK. Our work differs from these previous experiments in that we use exfoliation and mechanical stacking to couple an insulating magnetic layer ($\text{Cr}_2\text{Ge}_2\text{Te}_6$) to a non-magnetic topological insulator (BiSbTeSe_2), rather than growing the heterostructure by deposition. Using the stacking technique, we demonstrate anomalous Hall signals which reach the full quantized level of $e^2/2h$ for the parity anomaly state at temperatures up to 10 K. This is a factor of 100 times higher compared to the sole realization of a QAHE in a top-down-deposited proximity-coupled structure (15), and it is the first QAHE state in any materials system well above liquid helium temperature (4.2 K), enabling easy cooling. We also perform direct measurements of the electron chemical

potential versus carrier density which indicate a large exchange gap $\Delta = 10 \pm 2$ meV in the topological surface state of the BiSbTeSe₂, consistent with the high temperature scale for the quantization of the Hall signal. These results demonstrate a generalizable approach for realizing other high-temperature QAHE states, with potential applications for metrology, dissipationless charge transport, and topological quantum computation.

Results

The heterostructures we study contain thin exfoliated flakes of the van der Waals topological insulator BiSbTeSe₂ and the van der Waals magnetic insulator Cr₂Ge₂Te₆ encapsulated in hexagonal boron nitride (hBN) both above and below. A doped silicon substrate provides a back gate and a 100 nm layer of Ti/Pt serves as a top gate. The device geometry and the measurement setup are shown in Fig. 1(b-d). We choose the topological insulator BiSbTeSe₂ because it has a Dirac point well-positioned near the middle of bandgap between valence and conduction states, with a chemical potential near the Dirac point. The high quality of our BiSbTeSe₂ is reflected in a surface state mobility of 4000-4500 cm²/Vs and efficient tunability of the resistivity with gate voltage (37–39). Cr₂Ge₂Te₆ is a ferromagnet with perpendicular magnetic anisotropy and a Curie temperature around 50 K for thin flakes (40). We assemble the heterostructures using exfoliation and sequential pick-up techniques employed commonly for two-dimensional materials (for more details see Supplementary Material). The exfoliation and assembly are done in an inert environment inside an argon-filled glovebox. Electrical contact to the BiSbTeSe₂ layer is made via Pt electrodes pre-patterned on the bottom hBN layer, and after assembly all the layers are etched into Hall bars 8 μ m in total length and $w = 2$ μ m wide, with $L = 2$ μ m between the voltage probes used to measure the longitudinal resistance. The data reported in the main text are from a device that contains a BiSbTeSe₂ layer $t_{TI} = 10$ nm thick and a Cr₂Ge₂Te₆ layer 2.1 nm thick. Results from a second device are reported in the Supplementary Material.

Our layer stacks are similar to those reported previously in references (39, 41), but in those works the devices were not etched into well-defined Hall bars. The topological insulator layer extended laterally well beyond the magnetic layer thereby shunting the Hall signal and preventing quantitative determinations of the Hall conductivity.

Quantized anomalous Hall measurements

Figures 2(a) and (b) show the measured Hall resistance and longitudinal resistance at 4.5 K as a function of applied magnetic field swept out of plane, for a sequence of values of the top gate voltage near the Dirac point of the topological surface state of BiSbTeSe₂. The back gate is biased at -7 V, near the Dirac point of the bottom surface. The Hall resistance exhibits substantial hysteresis with large remanence at zero applied magnetic field. There is a small background slope with negative values for positive top-gate voltages V_{TG} and positive values for negative V_{TG} with a crossover near $V_{TG} = -0.5$ V, indicating that this is the bias region for which the Fermi level is gated through the Dirac point for the top surface state. The amplitude of the part of the Hall signal that switches is gate-dependent, with the maximum value near the Dirac point. The largest magnitude of the Hall resistance we observe is $R_{xy} = \pm 450$ Ω at $V_{TG} = -0.6$ V (Fig. 3(a)). The longitudinal resistance displays “butterfly”-shaped hysteresis curves as a function of swept magnetic field, also with maximum amplitude near the Dirac point. Similar butterfly-shaped longitudinal resistance curves have been seen in other QAHE systems, and the minima in the resistance are ascribed to enhanced conduction due to topological domain walls (30, 42).

The results in Fig. 2 are qualitatively similar to the previous measurements on unetched devices reported in (39, 41). However, the amplitudes are very different – the Hall resistances we report here are more than a factor of 50 greater than for the unetched devices, and the changes in longitudinal resistance are more than a factor of 10 greater. This is simply due to the fact that the transport measurements in the unetched devices were shunted by large areas of the topological insulator film that were not in contact with a magnetic layer. Here, because we use devices patterned into well-defined Hall bars, we are able to make an accurate measurement of the Hall and longitudinal resistivities associated with the topological insulator/magnet bilayer in isolation, and from these determine the Hall and longitudinal conductivities.

From the measured longitudinal resistance R_{xx} the two-dimensional longitudinal resistivity is calculated as $\rho_{xx} = R_{xx}w/L$, and the Hall resistivity is $\rho_{xy} = R_{xy}$. Based on inversion of the 2×2 resistivity matrix, the Hall and longitudinal conductivities can be calculated as

$$\sigma_{xy} = \frac{\rho_{xy}}{\rho_{xy}^2 + \rho_{xx}^2}; \quad \sigma_{xx} = \frac{\rho_{xx}}{\rho_{xy}^2 + \rho_{xx}^2}. \quad (1)$$

When converted into conductivities the data in Fig. 3(a) correspond to a Hall conductivity $\sigma_{xy} = 0.52 \pm 0.03 e^2/h$ (Fig. 3(b)). This value is consistent with the value for the parity anomaly state of $e^2/2h$. A level of quantization more precise than this is not expected for the parity anomaly state because the longitudinal resistivity is non-zero (due to the ungapped surface state on the side of the topological insulator film opposite from the magnetic layer) so that any uncertainties in the geometric factor w/L enter into the final result, and any spatial inhomogeneities in the current flow can also contribute to the Hall signal. For the parity anomaly state observed in magnetically-doped topological insulators, the level of quantization observed is also in the range $\sigma_{xy} = 0.48 - 0.52 e^2/h$ (10), very similar to our measurement.

The dependence of the transport data on changing top-gate voltage is plotted in Fig. 3(c,d), for measurements at 4.5 K and zero magnetic field. The Hall conductivity remains consistent with the quantized value $e^2/2h$ over the full range between the top-gate voltages of -1 V and 0 V. The longitudinal conductivity has a minimum in this same range of gate voltage but remains higher than $5 e^2/h$ due to conductance from the ungapped surface state on the interface opposite the magnetic layer. This value of σ_{xx} is significantly higher than for magnetically-doped topological insulators in the parity anomaly regime where $\sigma_{xx} = 0.5 - 1.2 e^2/h$, because the cleaner interface in the mechanically-assembled devices results in a higher mobility ($130 \text{ cm}^2/\text{Vs}$ (7) or $760 \text{ cm}^2/\text{Vs}$ (6) in magnetically-doped materials versus $4000-4500 \text{ cm}^2/\text{Vs}$ in the exfoliated BiSbTeSe_2 flakes (38)).

Figure 4(a) shows how the Hall conductivity as a function of swept magnetic field at $V_{TG} = -0.7$ V varies with temperature. These measurements were performed on the same device as for Fig. 2 and Fig. 3 but later in a separate cooldown, at which time the coercive field was slightly smaller. Due to the reduced coercive field, the Hall signal at zero applied magnetic field was reduced slightly compared to the full saturation value even at 2 K. Figure 4(b) summarizes the temperature dependence of the saturation value of Hall conductivity determined by fitting each set of measurements in Fig. 4(a) to a hyperbolic tangent function in the field range ± 0.05 T. The Hall conductivity remains in the range $(0.49 - 0.52) \pm 0.03 e^2/h$ up to 11 K, and drops below $0.45 e^2/h$ only above 15 K. It continues to decrease at higher temperatures but remains substantial almost all the way to the Curie temperature of the $\text{Cr}_2\text{Ge}_2\text{Te}_6$ near 50 K. A comparison of the temperature dependence to theory is described in the Supplementary Material. Based on this comparison, we conclude that the temperature dependence does not correspond to simple thermal activation across a temperature-independent exchange gap, but that the exchange gap decreases with increasing temperature in the regime where the Hall conductivity is temperature dependent. Nevertheless, from a fit to the Hall conductivity data at temperatures less than or equal to 15 K,

we can make a conservative estimate for a lower bound on the low-temperature exchange gap of $\Delta > 4.5 \pm 0.5$ meV (see Supplementary Material).

Chemical potential sensing

We can measure the exchange gap in the parity anomaly regime more directly by adapting a chemical-potential sensing technique developed for graphene double layers (43) and applied previously for measuring the magnetic-field-induced gap in a topological surface state (44). The technique uses the ungapped surface state on the bottom surface of the topological insulator film as a sensor layer. As the top and bottom gate voltages are tuned, the position of the peak in the longitudinal resistance is monitored (this peak is dominated by the ungapped surface state because the surface state at the magnetic interface is gapped). Due to capacitive coupling between the two surfaces of the topological insulator, changes in the chemical potential of the gapped surface state cause shifts in the position of the longitudinal resistance peak. After some algebra detailed in ref. (44), the electron chemical potential (μ_{top}) and carrier density (n_{top}) for the gapped interface on top of the topological insulator can both be determined from the gate voltages associated with the longitudinal resistance peak and the capacitance ratios within the device structure:

$$\mu_{top} = -\frac{C_B}{C_{TI}} eV'_{BG} \quad (2)$$

$$n_{top} = \frac{C_T}{e} \left(V'_{TG} + \left(\frac{1}{C_T} + \frac{1}{C_{TI}} \right) C_B V'_{BG} \right). \quad (3)$$

Here $C_{B,T,TI}$ correspond to the capacitive coupling constants (per unit area) of the bottom gate, the top gate, and the coupling between the two surfaces of the topological insulator, and $V'_{BG,TG} = V_{BG,TG} - V_{BG,TG}^0$ where V_{BG} is the back-gate voltage and $V_{BG,TG}^0$ are constants to normalize $n_{top} = 0$ when $\mu_{top} = 0$. The coupling factor between the two surfaces is calculated using the dielectric coefficient of BiSbTeSe₂ obtained from the literature ($\epsilon_{TI} = 32$) (44). Then $C_{TI} = \epsilon_0 \epsilon_{TI} / t_{TI} = 2.8$ $\mu\text{F}/\text{cm}^2$. The values of C_B and C_T are calculated similarly using the literature values for the dielectric coefficients of the boron nitride, Cr₂Ge₂Te₆, and SiO₂ (see Materials and Methods in SI for details). The results of this measurement are shown in Fig. 5, where the dots in Fig. 5(c) indicate the position of Dirac point of the bottom surface state as a function of swept V_{BG} for stepped values of V_{TG} . The value of V_{BG} corresponding to the resistance peak shows a jump near the double Dirac point of the system, indicating a gap in the top surface state. We can convert this into a plot of electron chemical potential versus carrier density using Eqs. (2) and (3) (Fig. 5(d)). The size of the exchange gap in the top surface state of the topological insulator is $\Delta(4.5\text{K}) = 10 \pm 2$ meV. This corroborates the high temperature scale we observe for the QAHE.

We can compare this result to exchange gaps determined for magnetically-doped topological insulators. Scanning tunneling microscope measurements on magnetically-doped Cr_{0.08}(Bi_{0.1}Sb_{0.9})_{1.92}Te₃ at 4.5 K indicated a distribution of exchange gap sizes from 9 meV to 48 meV centered around 30 meV (45). Angle-resolved photoemission measurements on (Bi_{0.84}Fe_{0.16})Se_{3.7} found a gap of approximately 50 meV (46). Despite these large spectroscopic gaps, the effective transport gaps determined by a thermal activation analysis of the longitudinal conductivity in magnetically-doped topological insulators are about a factor of 100 lower (e.g., 0.27 meV in CrO_x-capped Cr-modulation-doped (Bi_xSb_{1-x})₂Te₃ samples (47)). This difference in energy scales in the magnetically-doped topological insulators is generally attributed to low-energy states and Dirac-mass disorder induced by the magnetic dopants (3–5).

Conclusions and Outlook

We have shown that assembly of topological insulator/magnet samples by mechanical stacking allows realization of the parity anomaly state at temperatures up to at least 10 K, a new record value for any QAHE system and the first such system well above liquid helium temperature (4.2 K). This temperature scale is a factor of 100 higher compared to the only previous measurement of a proximity-induced QAHE in a topological insulator/magnet heterostructure grown by top-down deposition. We speculate that the reason for the difference in temperature scale compared to previous deposited proximity-coupled structures is that even a small amount of interfacial disorder in deposited samples can likely push the topological surface state away from the interface with the magnet, and therefore can disrupt the exchange coupling between the surface state and an adjacent magnet. Mechanical stacking of van der Waals layers provides pristine interfaces with no interfacial mixing.

Thus far, we have measured samples with a magnetic layer on only one surface of the topological insulator so that we realize the parity anomaly state. However, mechanical stacking will also allow fabrication of structures with magnetic layers on both sides of the topological insulator, providing a strategy to pursue high-temperature realizations of both the Chern insulator state and the axion insulator state. In addition to enabling high-temperature operation, samples made by mechanical stacking may have additional advantages relative to magnetically-doped topological insulators, e.g., much higher mobility for the topological surface state, the possibility to make separate electrical contacts to the top and bottom surfaces of a topological-insulator flake, and ease of making both top and bottom electrical gates to control carrier density and vertical electric field. Mechanically-assembled samples with quantum anomalous Hall effects above liquid helium temperature therefore provide a path for both more detailed fundamental research on the fascinating family of QAHEs and the potential to begin pursuing practical applications.

References and Notes

1. R. Yu, W. Zhang, H.-J. Zhang, S.-C. Zhang, X. Dai, Z. Fang, Quantized anomalous Hall effect in magnetic topological insulators. *Science* **329**, 61–64 (2010).
2. C.-X. Liu, S.-C. Zhang, X.-L. Qi, The quantum anomalous Hall effect: Theory and experiment. *Annual Review of Condensed Matter Physics* **7**, 301–321 (2016).
3. Y. Tokura, K. Yasuda, A. Tsukazaki, Magnetic topological insulators. *Nature Reviews Physics* **1**, 126–143 (2019).
4. H. Chi, J. S. Moodera, Progress and prospects in the quantum anomalous Hall effect. *APL Materials* **10**, 090903 (2022).
5. C.-Z. Chang, C.-X. Liu, A. H. MacDonald, Colloquium: Quantum anomalous Hall effect. *Reviews of Modern Physics* **95**, 011002 (2023).
6. C.-Z. Chang, J. Zhang, X. Feng, J. Shen, X. Zhang, M. Guo, K. Li, Y. Ou, P. Wei, L.-L. Wang, Z.-Q. Ji, Y. Feng, S. Ji, X. Chen, J. Jia, X. Dai, Z. Fang, S.-C. Zhang, K. He, Y. Wang, L. Lu, X.-C. Ma, Q.-K. Xue, Experimental observation of the quantum anomalous Hall effect in a magnetic topological insulator. *Science* **340**, 167–170 (2013).
7. C. Z. Chang, W. Zhao, D. Y. Kim, H. Zhang, B. A. Assaf, D. Heiman, S.-C. Zhang, C. Liu, M. H. Chan, J. S. Moodera, High-precision realization of robust quantum anomalous Hall state in a hard ferromagnetic topological insulator. *Nature Materials* **14**, 473–477 (2015).

8. A. Mahoney, J. Colless, S. Pauka, J. Hornibrook, J. Watson, G. Gardner, M. Manfra, A. Doherty, D. Reilly, On-chip microwave quantum Hall circulator. *Physical Review X* **7**, 011007 (2017).
9. H. Watanabe, Y. Hatsugai, H. Aoki, Half-integer contributions to the quantum Hall conductivity from single Dirac cones. *Phys. Rev. B* **82**, 241403 (2010).
10. M. Mogi, Y. Okamura, M. Kawamura, R. Yoshimi, K. Yasuda, A. Tsukazaki, K. Takahashi, T. Morimoto, N. Nagaosa, M. Kawasaki, Y. Takahashi, Y. Tokura, Experimental signature of the parity anomaly in a semi-magnetic topological insulator. *Nature Physics* **18**, 390–394 (2022).
11. M. Mogi, R. Yoshimi, A. Tsukazaki, K. Yasuda, Y. Kozuka, K. Takahashi, M. Kawasaki, Y. Tokura, Magnetic modulation doping in topological insulators toward higher-temperature quantum anomalous Hall effect. *Applied Physics Letters* **107**, 182401 (2015).
12. Y. Ou, C. Liu, G. Jiang, Y. Feng, D. Zhao, W. Wu, X.-X. Wang, W. Li, C. Song, L.-L. Wang, W. Wang, W. Wu, Y. Wang, K. He, X.-C. Ma, Q.-K. Xue, Enhancing the quantum anomalous Hall effect by magnetic codoping in a topological insulator. *Advanced Materials* **30**, 1703062 (2018).
13. H. Deng, Z. Chen, A. Wołoś, M. Konczykowski, K. Sobczak, J. Sitnicka, I. V. Fedorchenko, J. Borysiuk, T. Heider, Ł. Pluciński, K. Park, A. B. Georgescu, J. Cano, and L. Krusin-Elbaum, High-temperature quantum anomalous Hall regime in a $\text{MnBi}_2\text{Te}_4/\text{Bi}_2\text{Te}_3$ superlattice. *Nature Physics* **17**, 36–42 (2021).
14. H. T. Yi, D. Jain, X. Yao, S. Oh, Enhanced quantum anomalous Hall effect with an active capping layer. *Nano Letters* **23**, 5673–5679 (2023).
15. R. Watanabe, R. Yoshimi, M. Kawamura, M. Mogi, A. Tsukazaki, X. Yu, K. Nakajima, K. S. Takahashi, M. Kawasaki, Y. Tokura, Quantum anomalous Hall effect driven by magnetic proximity coupling in all-telluride based heterostructure. *Applied Physics Letters* **115**, 102403 (2019).
16. Y. Deng, Y. Yu, M. Z. Shi, Z. Guo, Z. Xu, J. Wang, X. H. Chen, Y. Zhang, Quantum anomalous Hall effect in intrinsic magnetic topological insulator MnBi_2Te_4 . *Science* **367**, 895–900 (2020).
17. C. Liu, Y. Wang, H. Li, Y. Wu, Y. Li, J. Li, K. He, Y. Xu, J. Zhang, Y. Wang, Robust axion insulator and Chern insulator phases in a two-dimensional antiferromagnetic topological insulator. *Nature Materials* **19**, 522–527 (2020).
18. M. Serlin, C. Tschirhart, H. Polshyn, Y. Zhang, J. Zhu, K. Watanabe, T. Taniguchi, L. Balents, A. Young, Intrinsic quantized anomalous Hall effect in a moiré heterostructure. *Science* **367**, 900–903 (2020).
19. A. L. Sharpe, E. J. Fox, A. W. Barnard, J. Finney, K. Watanabe, T. Taniguchi, M. Kastner, D. Goldhaber-Gordon, Emergent ferromagnetism near three-quarters filling in twisted bilayer graphene. *Science* **365**, 605–608 (2019).
20. G. Chen, A. L. Sharpe, E. J. Fox, Y.-H. Zhang, S. Wang, L. Jiang, B. Lyu, H. Li, K. Watanabe, T. Taniguchi, Z. Shi, T. Senthil, D. Goldhaber-Gordon, Y. Zhang, F. Wang, Tunable correlated Chern insulator and ferromagnetism in a moiré superlattice. *Nature* **579**, 56–61 (2020).

21. T. Li, S. Jiang, B. Shen, Y. Zhang, L. Li, Z. Tao, T. Devakul, K. Watanabe, T. Taniguchi, L. Fu, J. Shan, K. F. Mak, Quantum anomalous Hall effect from intertwined moiré bands. *Nature* **600**, 641–646 (2021).
22. J. Cai, E. Anderson, C. Wang, X. Zhang, X. Liu, W. Holtzmann, Y. Zhang, F. Fan, T. Taniguchi, K. Watanabe, Y. Ran, T. Cao, L. Fu, D. Xiao, W. Yao, X. Xu, Signatures of fractional quantum anomalous Hall states in twisted MoTe₂. *Nature* **622**, 63–68 (2023).
23. Y. Zeng, Z. Xia, K. Kang, J. Zhu, P. Knuppel, C. Vaswani, K. Watanabe, T. Taniguchi, K. F. Mak, J. Shan, Thermodynamic evidence of fractional Chern insulator in moiré MoTe₂. *Nature* **622**, 69–73 (2023).
24. H. Park, J. Cai, E. Anderson, Y. Zhang, J. Zhu, X. Liu, C. Wang, W. Holtzmann, C. Hu, Z. Liu, T. Taniguchi, K. Watanabe, J.-H. Chu, T. Cao, L. Fu, W. Yao, C.-Z. Chang, D. Cobden, D. Xiao, X. Xu, Observation of fractionally quantized anomalous Hall effect. *Nature* **622**, 74–79 (2023).
25. S. Bhattacharyya, G. Akhgar, M. Gebert, J. Karel, M. T. Edmonds, M. S. Fuhrer, Recent progress in proximity coupling of magnetism to topological insulators. *Advanced Materials* **33**, 2007795 (2021).
26. A. Grutter, Q. He, Magnetic proximity effects in topological insulator heterostructures: Implementation and characterization. *Physical Review Materials* **5**, 090301 (2021).
27. Y. Hou, J. Kim, R. Wu, Magnetizing topological surface states of Bi₂Se₃ with a CrI₃ monolayer. *Science Advances* **5**, 1874 (2019).
28. P. Li, Y. You, K. Huang, W. Luo, Quantum anomalous Hall effect in Cr₂Ge₂Te₆/Bi₂Se₃/Cr₂Ge₂Te₆ heterostructures. *Journal of Physics: Condensed Matter* **33**, 465003 (2021).
29. W. Luo, X.-L. Qi, Massive Dirac surface states in topological insulator/magnetic insulator heterostructures. *Phys. Rev. B* **87**, 085431 (2013).
30. P. Wei, F. Katmis, B. A. Assaf, H. Steinberg, P. Jarillo-Herrero, D. Heiman, J. S. Moodera, Exchange-coupling-induced symmetry breaking in topological insulators. *Phys. Rev. Lett.* **110**, 186807 (2013).
31. L. Alegria, H. Ji, N. Yao, J. Clarke, R. J. Cava, J. R. Petta, Large anomalous Hall effect in ferromagnetic insulator-topological insulator heterostructures. *Applied Physics Letters* **105**, 053512 (2014).
32. C. Tang, C.-Z. Chang, G. Zhao, Y. Liu, Z. Jiang, C.-X. Liu, M. R. McCartney, D. J. Smith, T. Chen, J. S. Moodera, J. Shi, Above 400-K robust perpendicular ferromagnetic phase in a topological insulator. *Science Advances* **3**, 1700307 (2017).
33. J. S. Lee, A. Richardella, R. D. Fraleigh, C.-x. Liu, W. Zhao, N. Samarth, Engineering the breaking of time-reversal symmetry in gate-tunable hybrid ferromagnet/topological insulator heterostructures. *npj Quantum Materials* **3**, 51 (2018).
34. X. Yao, B. Gao, M.-G. Han, D. Jain, J. Moon, J. W. Kim, Y. Zhu, S.-W. Cheong, S. Oh, Record high-proximity-induced anomalous Hall effect in (Bi_xSb_{1-x})₂Te₃ thin film grown on CrGeTe₃ substrate. *Nano Letters* **19**, 4567–4573 (2019).

35. M. Mogi, T. Nakajima, V. Ukleev, A. Tsukazaki, R. Yoshimi, M. Kawamura, K. S. Takahashi, T. Hanashima, K. Kakurai, T.-H. Arima, M. Kawasaki, Y. Tokura, Large anomalous Hall effect in topological insulators with proximitized ferromagnetic insulators. *Phys. Rev. Lett.* **123**, 016804 (2019).
36. L. J. Riddiford, A. J. Grutter, T. Pillsbury, M. Stanley, D. Reifsnnyder Hickey, P. Li, N. Alem, N. Samarth, Y. Suzuki, Understanding signatures of emergent magnetism in topological insulator/ferrite bilayers. *Phys. Rev. Lett.* **128**, 126802 (2022).
37. S. K. Chong, K. B. Han, A. Nagaoka, R. Tsuchikawa, R. Liu, H. Liu, Z. V. Vardeny, D. A. Pesin, C. Lee, T. D. Sparks, V. V. Deshpande, Topological insulator-based van der Waals heterostructures for effective control of massless and massive Dirac fermions. *Nano Letters* **18**, 8047–8053 (2018).
38. K.-B. Han, S. K. Chong, A. O. Oliynyk, A. Nagaoka, S. Petryk, M. A. Scarpulla, V. V. Deshpande, T. D. Sparks, Enhancement in surface mobility and quantum transport of $\text{Bi}_{2-x}\text{Sb}_x\text{Te}_{3-y}\text{Se}_y$ topological insulator by controlling the crystal growth conditions. *Scientific Reports* **8**, 17290 (2018).
39. V. Gupta, R. Jain, Y. Ren, X. S. Zhang, H. F. Alnaser, A. Vashist, V. V. Deshpande, D. A. Muller, D. Xiao, T. D. Sparks, D. C. Ralph, Gate-tunable anomalous Hall effect in a 3D topological insulator/2D magnet van der Waals heterostructure. *Nano Letters* **22**, 7166–7172 (2022).
40. C. Gong, L. Li, Z. Li, H. Ji, A. Stern, Y. Xia, T. Cao, W. Bao, C. Wang, Y. Wang, Z. Q. Qiu, R. J. Cava, S. G. Louie, J. Xia, X. Zhang, Discovery of intrinsic ferromagnetism in two-dimensional van der Waals crystals. *Nature* **546**, 265–269 (2017).
41. A. E. Llacsahuanga Allica, X.-C. Pan, I. Miotkowski, K. Tanigaki, Y. P. Chen, Gate-tunable anomalous Hall effect in stacked van der Waals ferromagnetic insulator–topological insulator heterostructures. *Nano Letters* **22**, 8130–8136 (2022).
42. J. G. Checkelsky, J. Ye, Y. Onose, Y. Iwasa, Y. Tokura, Dirac-fermion-mediated ferromagnetism in a topological insulator. *Nature Physics* **8**, 729–733 (2012).
43. S. Kim, I. Jo, D. Dillen, D. Ferrer, B. Fallahazad, Z. Yao, S. Banerjee, E. Tutuc, Direct measurement of the Fermi energy in graphene using a double-layer heterostructure. *Phys. Rev. Lett.* **108**, 116404 (2012).
44. V. Fatemi, B. Hunt, H. Steinberg, S. L. Eltinge, F. Mahmood, N. P. Butch, K. Watanabe, t. Taniguchi, N. Gedik, R. C. Ashoori, P. Jarillo-Herrero, Electrostatic coupling between two surfaces of a topological insulator nanodevice. *Phys. Rev. Lett.* **113**, 206801 (2014).
45. I. Lee, C. K. Kim, J. Lee, S. J. Billinge, R. Zhong, J. A. Schneeloch, T. Liu, T. Valla, J. M. Tranquada, G. Gu, J. C. S. Davis, JImaging Dirac-mass disorder from magnetic dopant atoms in the ferromagnetic topological insulator $\text{Cr}_x(\text{Bi}_{0.1}\text{Sb}_{0.9})_{2-x}\text{Te}_3$. *Proceedings of the National Academy of Sciences* **112**, 1316–1321 (2015).
46. Y. Chen, J.-H. Chu, J. Analytis, Z. Liu, K. Igarashi, H.-H. Kuo, X. Qi, S.-K. Mo, R. Moore, D. Lu, M. Hashimoto, T. Sasagawa, S. C. Zhang, R. Fisher, Z. Hussain, Z.-X. Shen, Massive Dirac fermion on the surface of a magnetically doped topological insulator. *Science* **329**, 659–662 (2010).

47. E. J. Fox, I. T. Rosen, Y. Yang, G. R. Jones, R. E. Elmquist, X. Kou, L. Pan, K. L. Wang, D. Goldhaber-Gordon, Part-per-million quantization and current-induced breakdown of the quantum anomalous Hall effect. *Phys. Rev. B* **98**, 075145 (2018).
48. A. Nagaoka, K. Yoshino, H. Taniguchi, T. Taniyama, H. Miyake. Growth of $\text{Cu}_2\text{ZnSnS}_4$ single crystal by traveling heater method. *Japanese Journal of Applied Physics*, **50**, 128001 (2011).
49. Miyake K. Sugiyama. Single Crystal Growth of Cu-III-VI₂ Semiconductors by THM. *Japanese Journal of Applied Physics*, **32**, 156–160 (1993).
50. A. Pierret, D. Mele, H. Graef, J. Palomo, T. Taniguchi, K. Watanabe, Y. Li, B. Toury, C. Journet, P. Steyer, V. Garnier, A. Loiseau, J.-M. Berroir, E. Bocquillon, G. Fève, C. Voisin, E. Baudin, M. Rosticher, B. Plaçais. Dielectric permittivity, conductivity and breakdown field of hexagonal boron nitride. *Materials Research Express* **9**, 065901 (2022).
51. J. Escolar, N. Peimyoo, M. F. Craciun, H. A. Fernandez, S. Russo, M. D. Barnes, F. Withers. Anisotropic magnetoconductance and Coulomb blockade in defect engineered $\text{Cr}_2\text{Ge}_2\text{Te}_6$ van der Waals heterostructures. *Phys. Rev. B* **100**, 054420 (2019).

Acknowledgments: We acknowledge helpful discussions with Nitin Samarth, Chaoxing Liu, Thow Min Cham, and Katja Nowack and technical assistance from Xiaoxi Huang.

Funding:

Air Force Office of Scientific Research/MURI project 2DMagic, grant FA9550-19-1-0390 (RJ, VG, DCR)

US National Science Foundation grant DMR-2104268 (VG, BH, DCR)

SUPREME, one of seven centers in JUMP 2.0, a Semiconductor Research Corporation program sponsored by DARPA (MR)

Kavli Institute at Cornell Graduate Engineering Fellowship (RJ)

US National Science Foundation under the Quantum Leap Big Idea Grant 1936383 (HMS, HFA, AV, VVD, TDS)

Japan Society for the Promotion of Science/KAKENHI grants 21H05233 and 23H02052 (KW, TT)

World Premier International Research Center Initiative (WPI), MEXT, Japan (KW, TT)

The shared facilities of the Cornell Center for Materials Research, supported by the US National Science Foundation via grant DMR-1719875

The shared facilities of the Cornell NanoScale Facility, a member of the National Nanotechnology Coordinated Infrastructure, supported by the US National Science Foundation via grant NNCI-2025233

Author contributions:

Device fabrication, measurements, and data analysis: RJ, MR

Initiation of recipes uses for the device fabrication: VG

Assistance with device fabrication and data analysis: BH

Growth of BiSbTeSe₂ crystals: HMS, HFA, AV, VVD, TDS

hBN crystals: KW, TT

Supervision and assistance with data analysis: DCR

Writing – original draft: RJ, MR, DCR

Writing – review: all authors

Competing interests: Authors declare that they have no competing interests.

Data and materials availability: All data from the main text and supplementary materials will be deposited in the Zenodo repository prior to publication, and a link will be provided upon acceptance of the paper.

Supplementary Materials

Materials and Methods

Supplementary Text: Data From an Additional Device

Figs. S1 to S5

Table 1

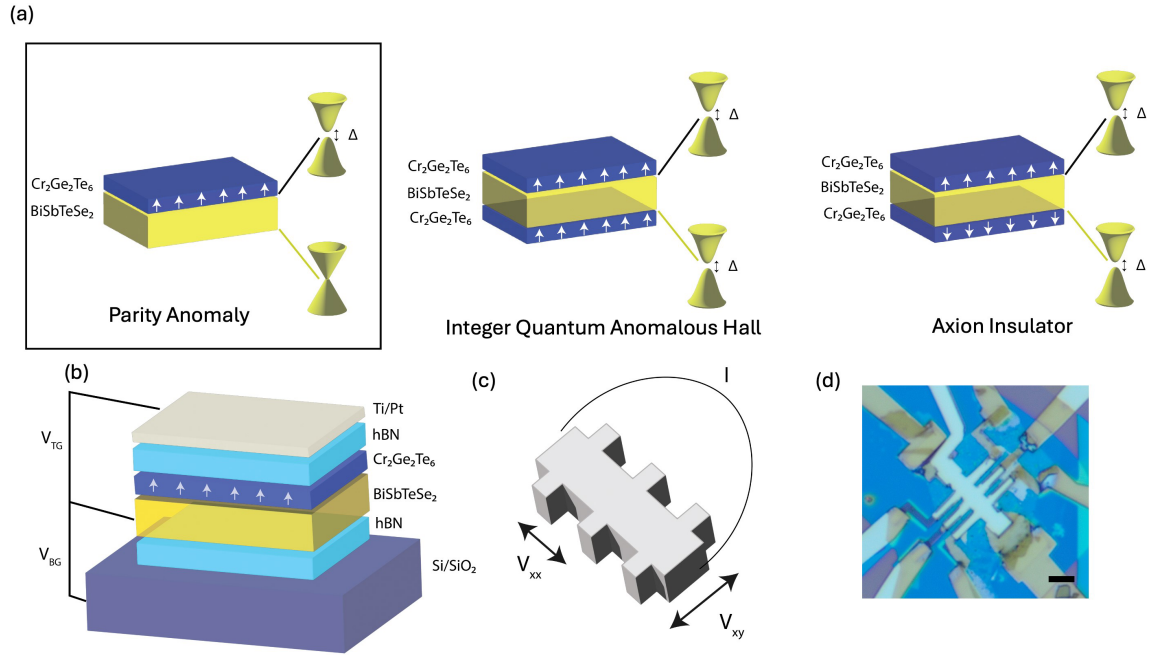


Fig. 1 Parity anomaly state, measurement geometry, and heterostructure used in this work. (a) Device configurations corresponding to the parity anomaly state, the integer quantum anomalous Hall state, and the axion insulator state, showing the gapped and un-gapped topological surface states. The exchange gap is shown as Δ . (b) Heterostructure consisting of the van der Waals magnet $\text{Cr}_2\text{Ge}_2\text{Te}_6$ and the topological insulator BiSbTeSe₂ double-encapsulated in hBN (thicknesses not to scale). The top layer is a metallic gate (Ti/Pt) and the bottom gate is Si/SiO₂. (c) Hall-bar geometry used in the work. V_{xy} , V_{xx} and I represent transverse voltage, longitudinal voltage, and applied current, respectively. (d) Top view of the device after etching into the Hall bar geometry. Scale bar for the image is 4 μm .

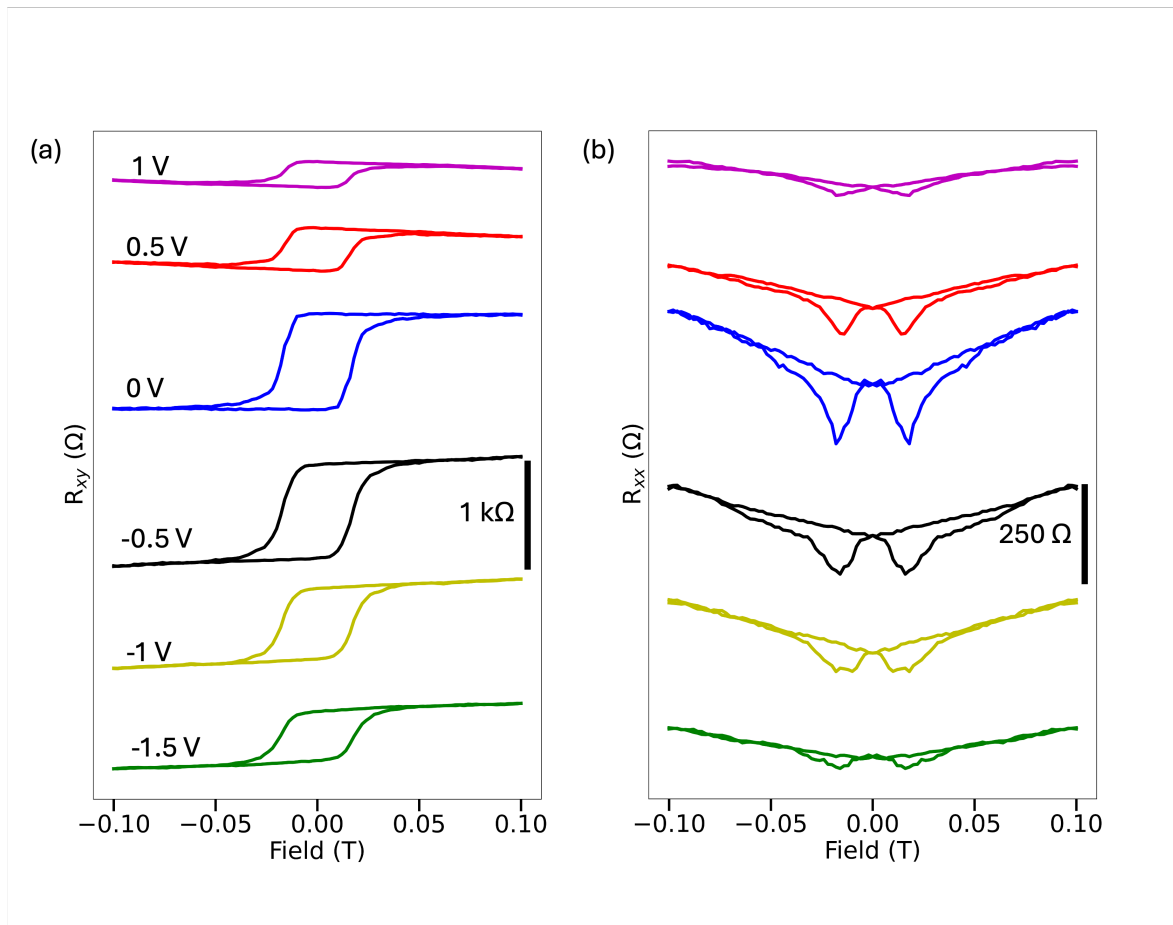


Fig. 2 Anomalous Hall resistance and longitudinal resistance at 4.5 K as a function of out-of-plane magnetic field at different values of top gate voltage. (a) Anomalous Hall resistance. (b) Longitudinal resistance. Curves in both panels are offset vertically. The zero-field values of R_{xx} are plotted in Fig. 3(c).

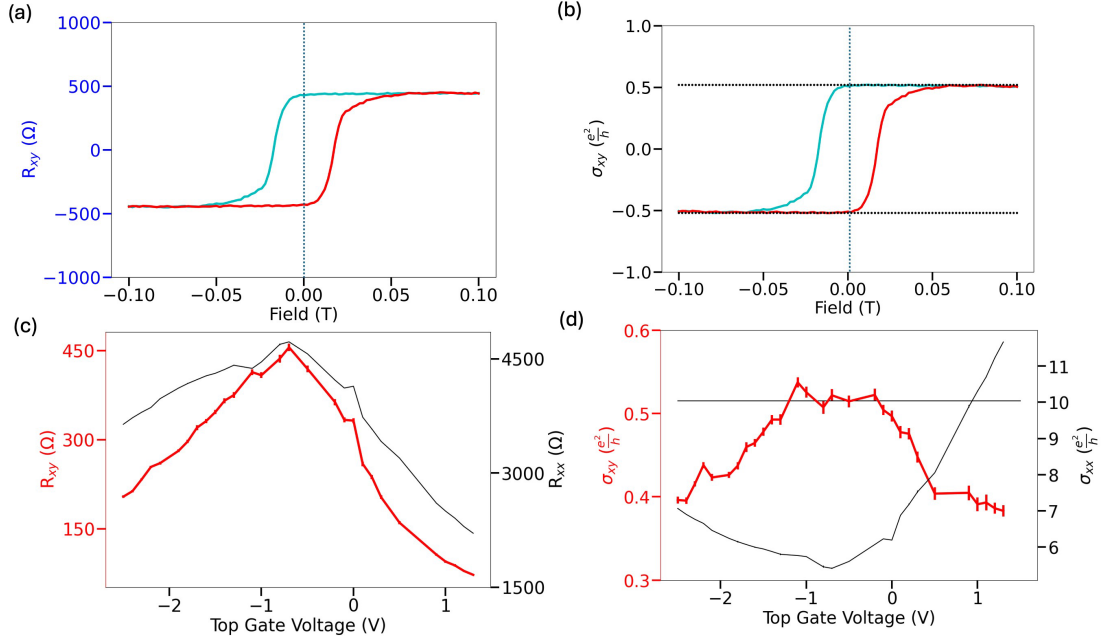


Fig. 3 Hall measurements at 4.5 K as a function of top gate voltage. (a,b) Magnetic field sweep of the Hall resistance along with the corresponding Hall conductivity at a top gate voltage of -0.6 V, the value of V_{TG} for which the chemical potential is near the middle of the exchange gap. (c) Hall and longitudinal resistances at 4.5 K and zero applied magnetic field as a function of top gate voltage (d) Hall and longitudinal conductivities at zero applied magnetic field as a function of top gate voltage. When the chemical potential lies inside the exchange gap, the Hall conductivity is quantized close to $e^2/2h$. The current excitation used for this measurement is 200 μ A and V_{BG} is fixed at -7 V.

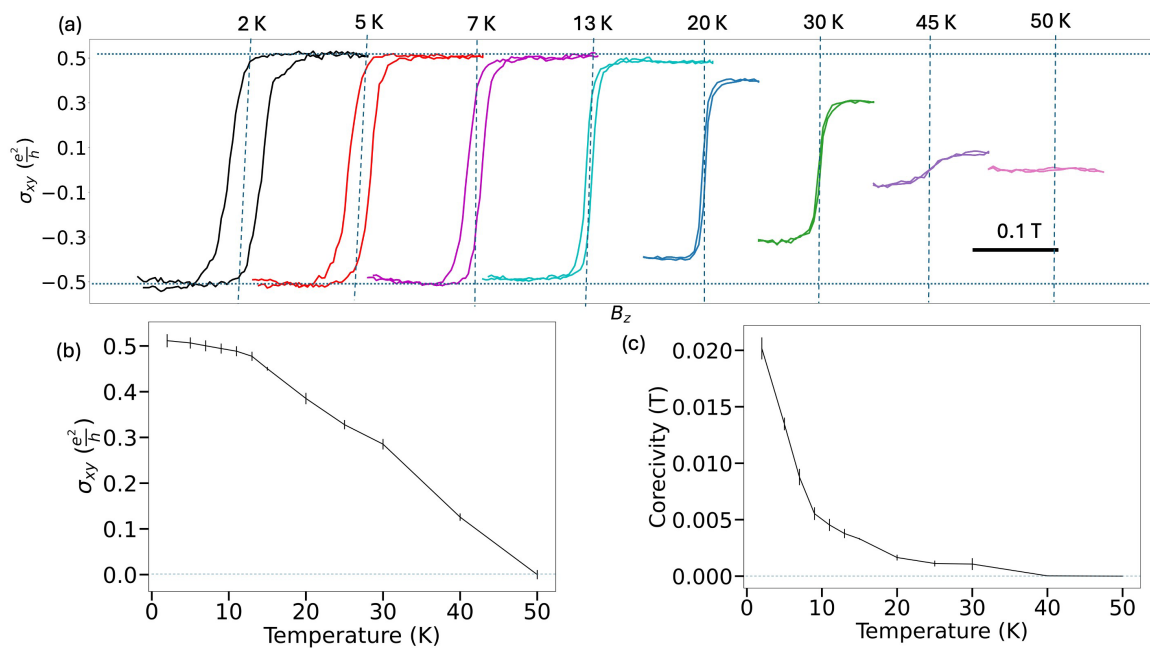


Fig. 4 Temperature dependence of the anomalous Hall conductivity. (a) Hall conductivity as a function of magnetic field for various temperatures at a fixed top-gate voltage $V_{TG} = -0.7$ V. (b) Temperature dependence of the Hall conductivity, corresponding to the saturated value of σ_{xy} in small applied magnetic field. The Curie temperature for the magnet is around 50 K. (c) Temperature dependence of the magnetic coercivity from the plots in panel (a).

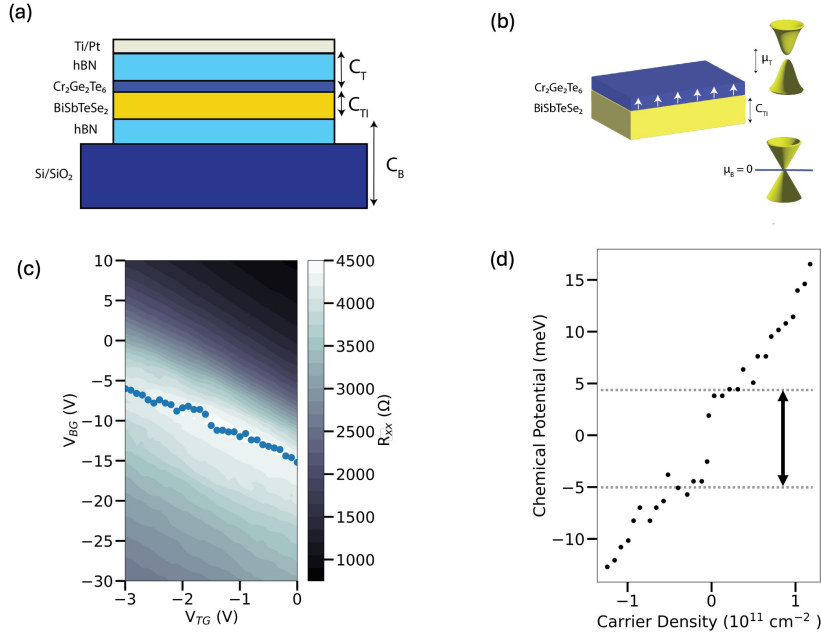


Fig. 5 Direct measurement of the exchange gap (a,b) Schematic for the chemical potential sensing experiment (layer thicknesses not to scale). The bottom topological surface state acts as the sensor layer to detect changes in the chemical potential of the top surface state. (c) Chemical potential sweep indicating the presence of a gap in the topological surface state near the double Dirac point. In the scans the bottom gate is swept as a function of stepping the top gate voltage. The dots indicate the position of the resistance peak as a function of bottom gate voltage. (Note that the gate voltages corresponding to peak resistance are shifted slightly relative to Fig. 4; this change happened upon an excursion to a large back-gate voltage, but was otherwise stable.) (d) The Dirac peak position converted into chemical potential μ_{top} versus carrier density n_{top} using Eqs. (2) and (3). The capacitance values used for the conversion are $C_{TI} = 2800$ nF/cm², $C_B = 11$ nF/cm², $C_T = 130$ nF/cm².

Supplementary Material: A quantized anomalous Hall effect above 4.2 K in stacked topological insulator/magnet bilayers

1 Materials and Methods

1.1 Steps for Device Fabrication

1. Fabrication of Contact Electrodes

- (a) Exfoliate hexagonal Boron Nitride (hBN) onto pre-patterned alignment grids and identify suitable flakes using optical microscopy (S1(a)).
- (b) Design Hall-bar contacts with a channel length of $8\mu\text{m}$ and a width of $3\mu\text{m}$ to be contained on the hBN flake.
- (c) For electron-beam lithography, spin-coat a bilayer of resists onto the wafer:
 - i. PMMA 495 A4, spun at 2000 RPM for 60 seconds then baked at 170°C for 2 minutes,
 - ii. PMMA 950 A4, spun at 2000 RPM for 60 seconds then baked at 170°C for 2 minutes.
- (d) Perform electron beam lithography to pattern inner contact electrodes using a Zeiss Supra scanning electron microscope coupled with a Nabyty nanometer pattern generating system with an acceleration voltage of 20 kV.
- (e) Develop the resist using a chilled mixture of Isopropanol(IPA)/DI Water (3:1 ratio by volume).
- (f) Deposit Pt(8 nm) for inner electrodes using an Angstrom electron-beam evaporator (S1(b)).
- (g) Lift-off excess metal in a bath of acetone followed by an IPA rinse.
- (h) Repeat steps 1(c)-1(e) to pattern outer contact electrodes.
- (i) Evaporate Ti(15 nm)/Pd(30 nm) for the outer electrodes and perform lift-off as previously described (S1(c)).
- (j) Clean the device channel and electrodes of residue by performing contact atomic force microscopy (AFM) over a large scan area ($\approx 40\mu\text{m} \times 40\mu\text{m}$).

2. Material Exfoliation and Transfer

- (a) Exfoliate hBN onto Si/SiO₂ and identify appropriate flakes using optical microscopy.
- (b) Exfoliate flakes of BiSbTeSe₂ (BSTS) and Cr₂Ge₂Te₆ (CGT) using conventional scotch tape methods in an Argon filled glovebox with O₂ and H₂O concentrations below 0.1 ppm and identify flakes using optical microscopy.
- (c) Pick up the flakes in top-to-bottom order (hBN \rightarrow CGT \rightarrow BSTS) using a dry-transfer polycarbonate/PDMS stamp and transfer to the contact electrodes (S1(d)).
- (d) Remove the polycarbonate by soaking in chloroform for ≈ 2 hours.
- (e) Use AFM to measure the thickness of each layer in the device stack and ensure cleanliness of stack.
- (f) Store the device in the inert Argon environment when not performing measurements or fabrication to minimize exposure to atmospheric conditions.

3. Top Gate Deposition

- (a) Repeat steps 1(c) - 1(e) to pattern the top-gate in a design that covers the channel width and regions overlying contact electrodes.
- (b) Deposit alternating layers of Ti(10 nm)/Pt(40 nm) 2 times in a sputtering system (S1(e)).
- (c) Lift-off excess metal using acetone, gently flushing with acetone to avoid damaging the gate, then rinsing in IPA.

4. Etching into Hall-Bar Geometry

- (a) For lithography prior to etching, spin-coat a bilayer of resists onto the wafer:
 - i. PMMA 50 A8, spun at 2000 rpm for 60 seconds then baked at 170° C for 2 minutes,
 - ii. PMMA 950 A4, spun at 2000 rpm for 60 seconds then baked at 170° C for 2 minutes.
- (b) Repeat steps 1(d) and 1(e) to pattern an etching region onto the device that removes any shorting regions of BSTS away from the channel and contact electrodes.
- (c) Etch the hBN using a reactive ion etching tool:
 - i. Use a CHF₃/O₂ plasma at a chamber pressure of 50 mTorr and forward power of 50 W for 30 seconds,
 - ii. Examine the device under an optical microscope to determine if there is remaining hBN,
 - iii. Repeat the previous two steps 2-4 times depending on the thickness of the hBN until the hBN has been etched away entirely, revealing the exposed CGT and BSTS.
- (d) Etch the CGT and BSTS using a wet etch bath composed of DI H₂O:H₂O₂:H₃PO₄ (Phosphoric Acid) in a 9:3:1 ratio by volume for approximately 1 minute then rinse in IPA.
- (e) Examine the device under an optical microscope and if necessary, etch until the exposed BSTS and CGT is no longer visible (S1(f)).

1.2 Measurements.

The resistance measurements were carried out using a Keithley 6221 Source Meter to apply a 200 nA current bias at the frequency of 99.97 Hz, and measured using Signal Recovery Lockin Amplifier 7265 DSP. The top and bottom gate voltages were applied using Keithley 2400 source meters.

1.3 Capacitance Calculations.

The capacitance for the top gate is calculated using the capacitance of the top boron nitride flake and the CGT flake in series.

$$C_T = \frac{C_{\text{top-hBN}}C_{CGT}}{(C_{\text{top-hBN}} + C_{CGT})}$$

The capacitance of the bottom gate is calculated using the capacitance of the SiO₂ and the bottom hBN flake in series.

$$C_B = \frac{C_{SiO_2}C_{\text{bottom-hBN}}}{(C_{SiO_2} + C_{\text{bottom-hBN}})}$$

The capacitance of the individual layers is calculated using the $C = \frac{k\epsilon_0}{d}$ where d is the thickness and k is the dielectric coefficient.

1.4 Growth and characterization of the BiSbTeSe₂ crystals

1.4.1 Ampoule Preparation

Bismuth (Bi), antimony (Sb), tellurium (Te), and selenium (Se) were sourced with a purity level of 5N grade from Sigma-Aldrich Co. To prepare the ampoule, quartz tubes (outer diameter of 1.2 cm, inner diameter of 0.8 cm) from Thermo Fisher Scientific Chemicals, Inc., were used. The quartz tubes were initially sealed at one end into a conical form, and the inner surface was coated with a carbon film through the pyrolysis of acetone. This coating acted as a protective barrier, preventing any potential reaction between the raw materials and the quartz during the heating process. The materials were

weighed according to a 1:1:1:2 molar ratio of Bi:Sb:Te:Se, yielding a total mixture weight of 3 g. The prepared materials were placed inside the tube, which was subsequently flushed with argon gas multiple times to remove atmospheric air. Afterward, the tube was evacuated to create a vacuum environment, achieving a pressure below 10^{-6} torr. Once the desired vacuum level was reached, the quartz tube was sealed, forming an ampoule with a final length of approximately 8–9 cm.

1.4.2 Bridgman Growth

The crystal growth was performed using a vertical Bridgman furnace equipped with three heating zones (48). The ampoule, suspended vertically by a thin string connected to a motion controller, was positioned above the topmost heating zone. The temperatures of the furnace zones were set to 670°C (warm zone), 770°C (hot zone), and 500°C (cold zone), in descending order from top to bottom (38). The temperature profile is illustrated in Fig. S2. The purpose of the top heating zone was to preheat the ampoule, preventing the condensation of Se vapor along the tube walls (49). The ampoule was lowered into the furnace at a controlled rate of 0.6 cm/day, facilitating slow and controlled crystal growth along the vertical temperature gradient.

1.4.3 Characterization of the Crystals

Following crystal growth, the samples were carefully cleaved along their natural crystallographic planes. The exposed crystal surfaces were characterized using energy-dispersive X-ray spectroscopy (EDS) to determine the elemental composition. EDS measurements were carried out using an EDAX detector integrated with a FEI Quanta 600 scanning electron microscope (SEM), operated at an acceleration voltage of 15 kV. The technique provided high-resolution mapping of the distribution of Bi, Sb, Te, and Se elements across the sample.

1.5 Temperature Dependence of Hall Conductivity

We will consider the case that the Fermi energy is located in the middle of the exchange gap ($\Delta =$ full gap), so that at zero temperature the Hall conductivity has the saturated value for the parity anomaly state, $\sigma_{xy}(T = 0) = e^2/2h$. As a function of increasing temperature, the magnitude of the Hall conductivity will decrease due to thermal activation of carriers from the valence band to the conduction band. If we assume that the exchange gap and the form of the Berry curvature are temperature-independent, the change in the Hall conductivity as a function of temperature can be written as

$$\Delta\sigma_{xy} = -2\frac{e^2}{h} \int_{B.Z.} \frac{d^2k}{(2\pi)^2} \Omega(k) f(E)$$

where $\Omega(k)$ is the Berry curvature as a function of wavevector k and $f(E)$ the Fermi function as a function of energy. The factor of two denotes the contribution from both unfilled and filled bands. Integration over angle in polar coordinates yields

$$\Delta\sigma_{xy} = -2\frac{e^2}{h} \int_0^\infty k dk \frac{2\pi}{(2\pi)^2} \Omega(k) f(E) = -2\frac{e^2}{h} \int_0^\infty k dk \Omega(k) f(E).$$

The dispersion of the gapped surface state has the form

$$E = \sqrt{(\hbar v_f k)^2 + \left(\frac{\Delta}{2}\right)^2}$$

so that a change of variables from k to the energy E can be achieved via

$$dE = \frac{\hbar^2 v_f^2 k dk}{\sqrt{(\hbar v_f k)^2 + \left(\frac{\Delta}{2}\right)^2}}$$

$$k dk = E dE \frac{1}{\hbar^2 v_f^2}.$$

The Berry curvature depends on the exchange gap and carrier energy with the form

$$\Omega = \frac{\hbar^2 v_f^2 \Delta}{4E^3}.$$

Thus the change Hall conductivity from the zero-temperature value can be expressed as an integral over energy in the form

$$\Delta\sigma_{xy} = -\Delta \frac{e^2}{h} \int_{\frac{\Delta}{2}}^{\infty} dE \frac{f(E)}{E^2} = -\Delta \frac{e^2}{h} \int_{\frac{\Delta}{2}}^{\infty} dE \frac{1}{E^2(1 + e^{\beta E})}$$

This can be simplified as

$$\Delta\sigma_{xy} = -\left(\frac{\Delta}{2}\right) \beta \frac{e^2}{h} \int_{(\frac{\Delta}{2})\beta}^{\infty} dx \frac{1}{x^2(1 + e^x)}. \quad (1)$$

This final equation can be integrated numerically to obtain the predicted temperature dependence (again, this form assumes that the exchange gap is temperature-independent). In Fig. S4 we have fitted this form to the measured data up to 15 K – above 15 K the Hall conductivity begins to drop much more sharply than predicted by this simple form, indicating that the exchange gap is not temperature-independent. The fit indicates the temperature dependence of the Hall conductivity up to 15 K can be fitted reasonably with an exchange gap parameter of $\Delta = 4.5 \pm 0.5$ meV. This value should be taken only as a lower bound on the zero-temperature exchange gap, because the gap may already be decreasing with increasing temperature below 15 K, and it is also possible that the Fermi energy was not truly centered in the middle of the exchange gap during the temperature-dependent measurements. This lower bound from the temperature-dependent measurements is therefore consistent with the exchange gap determined directly from the chemical-potential sensing measurement described in the main text, $\Delta(4.5 \text{ K}) = 10 \pm 2$ meV.

2 Data From an Additional Device

Data from a second device with different dimensions are shown in Figure S3. The dimensions for this device are a width $w = 2 \mu\text{m}$ and length $L = 3 \mu\text{m}$ between the voltage probes used to measure the longitudinal resistance.

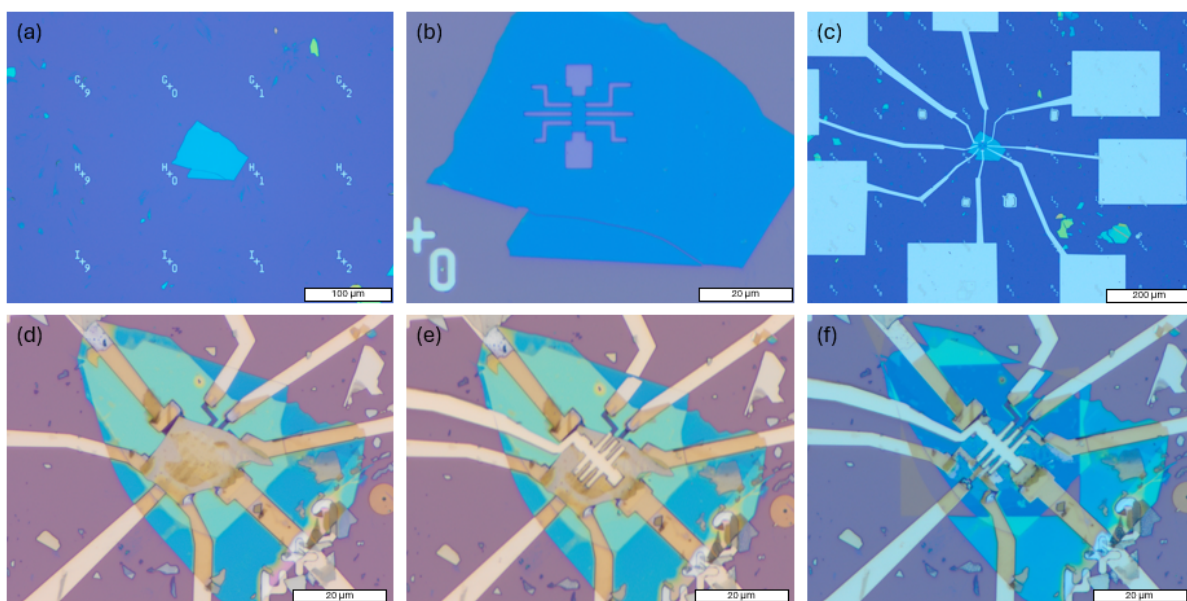


Figure S1: **Optical images of the fabrication process.** Images of the fabrication of electrodes for one device ((a)-(c)) and the subsequent creation of a top gate and etching into a Hall-bar geometry for a second device ((d)-(f)). Scale bars are 100 μm in (a), 20 μm in (b, d, e, and f), and 200 μm in (c).

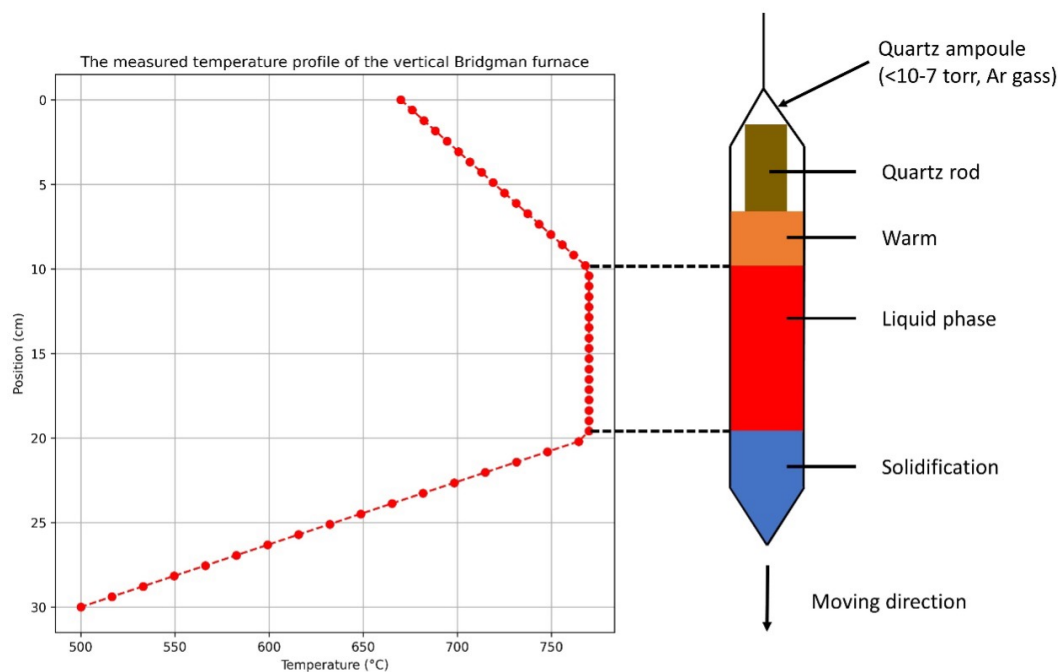


Figure S2: **The measured temperature profiles of the vertical Bridgman furnace**

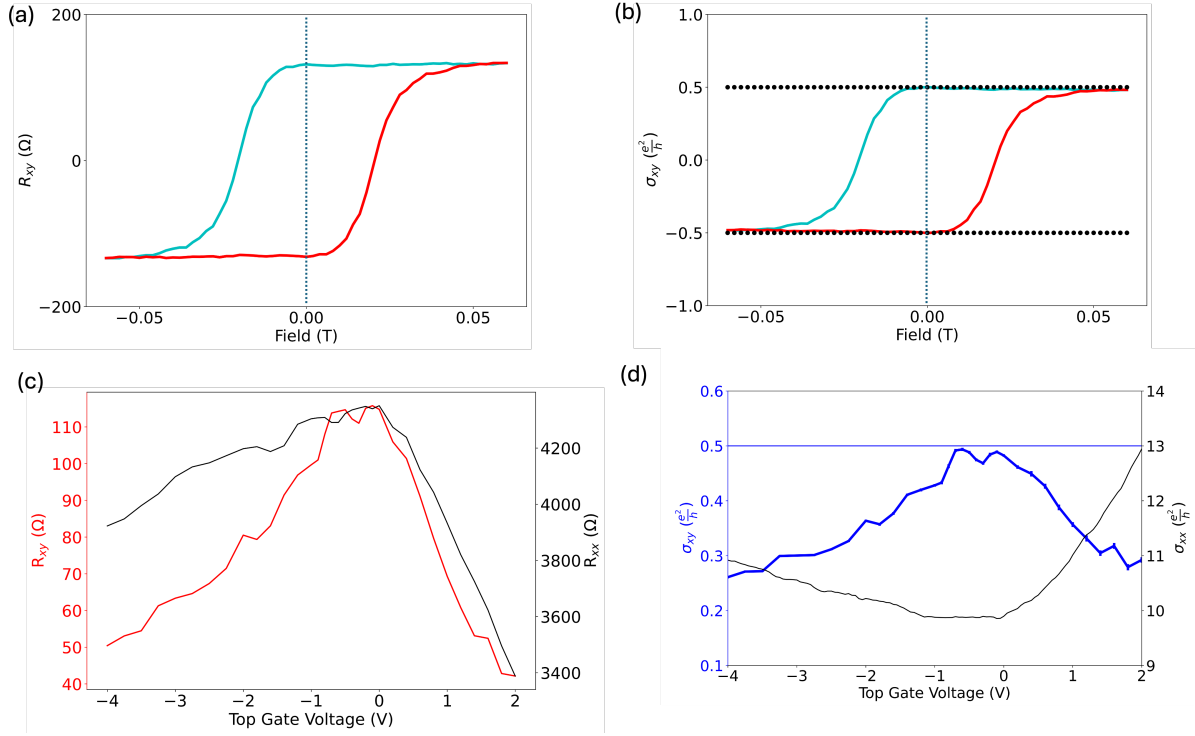


Figure S3: **Hall measurements at 4.5 K as a function of top gate voltage for a second device.** (a,b) Magnetic field sweep of the Hall resistance and Hall conductivity at a top gate voltage of -0.1 V, the value of V_{TG} for which the chemical potential is near the middle of the exchange gap. (c) Hall and longitudinal resistances at 4.5 K and zero applied magnetic field as a function of top gate voltage. (d) Hall and longitudinal conductivities at zero applied magnetic field as a function of top gate voltage. When the chemical potential lies inside the exchange gap, the Hall conductivity is quantized close to $e^2/2h$. The current excitation used for this measurement is $200 \mu\text{A}$.

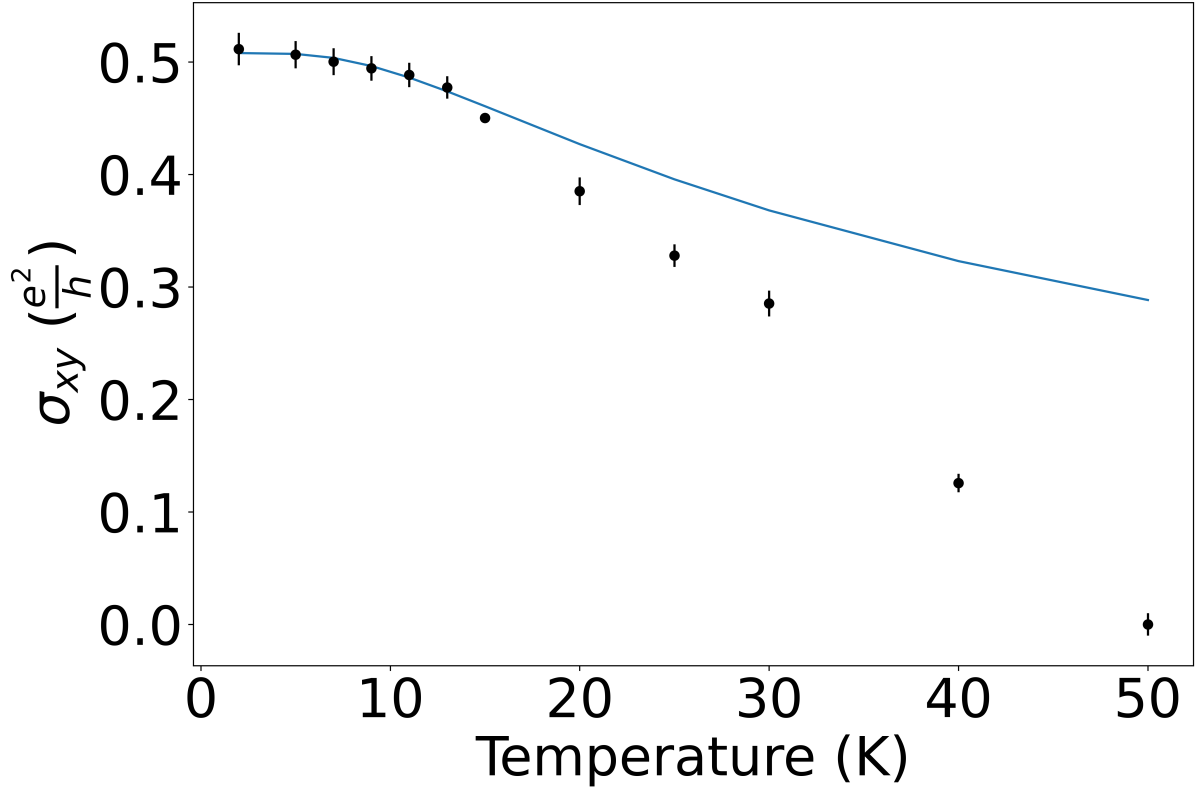


Figure S4: **Temperature dependence of the Hall conductivity** The circles are the data shown in the Fig. 4(b) in the main manuscript. The blue line is the fit of the data at temperatures ≤ 15 K to Eq. (3) of the Supplementary Material. We estimate a lower bound for the low-temperature exchange gap of $\Delta = 4.5 \pm 0.5$ meV from this fit. (See Section 4 of the Supplementary Material for the details of the analysis.)

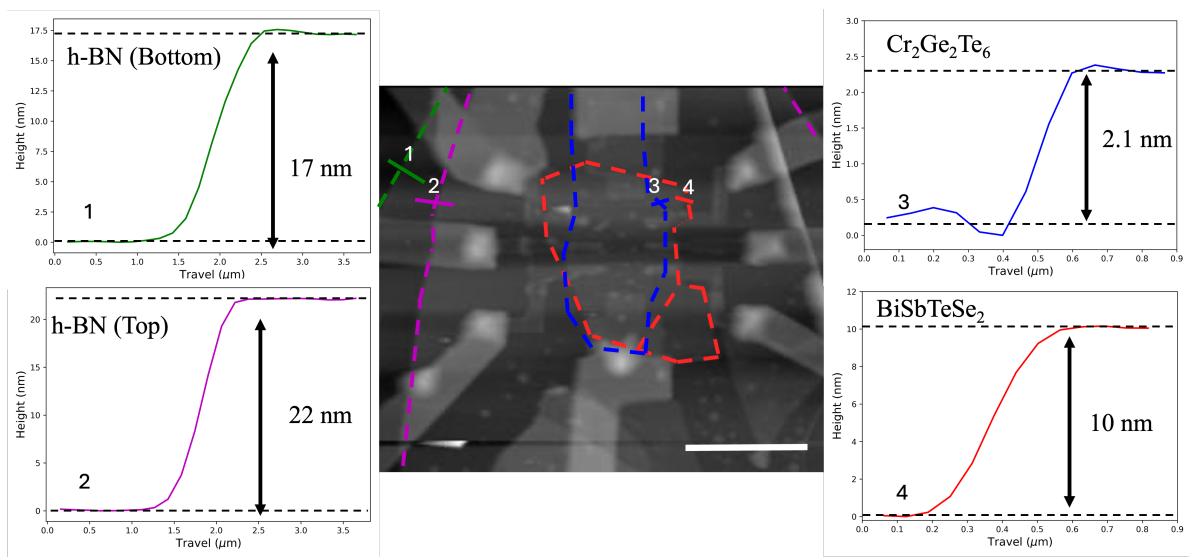


Figure S5: Atomic force microscope image of the device analyzed in the main text. The traces along 1, 2, 3, and 4 represent traces along the edge of bottom hBN, top hBN, Cr₂Ge₂Te₆, and BiSbTeSe₂ respectively. The scale bar for the image in the middle is 10 μm.

Material	k (Dielectric constant)	d (thickness)
Top hBN (<i>50</i>)	3.4	22 nm
Cr ₂ Ge ₂ Te ₆ (<i>51</i>)	4	2.1 nm
BiSbTeSe ₂ (<i>44</i>)	32	10 nm
Bottom hBN	3.4	17 nm
SiO ₂	3.9	285 nm

Table 1: Dielectric coefficients for materials used in the heterostructure.